Hydrogeology Journal (2023) 31:1647–1664
https://doi.org/10.1007/s10040-023-02638-1

PAPER

Joint hydrofacies-hydraulic conductivity modeling based on a constructive spectral algorithm constrained by transient head data

Dany Lauzon[1] · **Denis Marcotte**[1]

Received: 20 September 2022 / Accepted: 21 April 2023 / Published online: 20 July 2023

Abstract
A constructive spectral method is presented to jointly calibrate hydrofacies and hydraulic conductivity to transient pressure heads. The method iteratively constructs Gaussian random fields to model the spatial correlation of hydraulic conductivity and hydrofacies using pluriGaussian simulation. Borehole conditioning is done quickly by replacing the slow Gibbs sampler method with an approach that is based on calibrating the underlying Gaussian fields that are subject to inequality constraints. Calibration to transient pressure heads is performed by shallow optimization of the phase vectors of the continuous spectral method. A parameterization technique makes it possible to reduce phase vector optimization from multivariate to univariate. The algorithm is tested on two-dimensional (2D) and 3D synthetic regional aquifers made of three hydrofacies. It reduced the objective function by one order of magnitude in one hundred iterations. The tests on the 2D aquifers indicated that the transient hydraulic heads alone cannot provide much information about hydrofacies. However, combining them with hydrofacies observations from boreholes results in improved hydrofacies identification compared to when only borehole data are used. Similar results were obtained in the 3D aquifer case, although the improvement in aquifer identification was less pronounced. The spectral method presented makes it possible to calibrate complex aquifers to transient heads using a limited number of calls to the flow simulator. Doing so helps to characterize sub-surface heterogeneity and assess the uncertainty and geological risks associated with groundwater flow.

Keywords Geostatistics · Inverse modeling · Stochastic hydrogeology · Data assimilation · Parameter uncertainty assessment

Introduction

The characterization of groundwater flow parameters is critical for understanding complex aquifer systems (Bárdossy and Hörning 2015; Benoit et al. 2017; Benoit et al. 2020; Khambhammettu et al. 2020). Having heterogeneous hydrogeological parameter values renders modeling complex since data are usually sparsely available (Pasquier and Marcotte 2006). When a groundwater system is modeled using hydrofacies, the proportions and connectivity of hydrofacies are essential to assess a hydrogeological system's response to external perturbations such as pumping tests, a significant influx of precipitation, or the transportation of contaminants (Benoit et al. 2017). Since only incomplete knowledge is available about the geological system, calibrating the groundwater flow model requires solving an inverse problem (Tarantola 2005). The objective is to determine the unknown parameters (e.g., hydraulic conductivity, porosity, compressibility, the location of hydrofacies) while ensuring the state variables (e.g., transient hydraulic heads, geochemical concentration, travel time between wells, tracer test responses) are faithfully reproduced.

Parameter uncertainty (e.g., hydrogeological parameter range, spatial heterogeneity, hydrofacies proportions, hydrofacies architectures, boundary conditions) need to be adequately characterized (Chilès and Delfiner 2012). If some model parameters exhibit spatial correlation, the inverse problem can be solved using geostatistical inversion methods (Carrera et al. 2005; Bárdossy and Hörning 2015).

✉ Dany Lauzon
dany.lauzon@polymtl.ca

[1] Civil, Geological and Mining Engineering Department, Polytechnique Montréal, P.O. Box 6079 Station Centre-Ville, Montréal, Québec H3C 3A7, Canada

Hydrofacies uncertainty may be simulated using a variety of geostatistical methods (dell'Arciprete et al. 2011) such as multiple-point simulation (Strebelle 2002; Huysmans and Dassargues 2009; Mariethoz et al. 2010b), object-based simulation (Allard et al. 2005; Pyrcz et al. 2009), transition probability-based methods (D'Or 2003; Allard et al. 2011; Benoit et al. 2017), and pluriGaussian simulation (Armstrong et al. 2011; Le Blévec et al. 2017). Continuous variables such as hydraulic conductivity, on the other hand, may be simulated using geostatistical simulation methods that are based on the Gaussian hypothesis, like sequential Gaussian simulation (Deutsch 1992), discrete spectral methods (Dietrich and Newsam 1993; Chilès and Delfiner 1997; Le Ravalec et al. 2000) and continuous spectral methods (Shinozuka 1971; Shinozuka and Jan 1972; Shinozuka and Deodatis 1996; Lantuéjoul 2002; Emery et al. 2016). Many of these simulation methods have been combined in perturbation mechanisms for inverse modeling (Kirkpatrick et al. 1983; Marsily et al. 1984; Gómez-Hernández et al. 1997; Hu 2000; Mariethoz et al. 2010a; Bárdossy and Hörning 2015; Hörning and Bárdossy 2018; Rezaee and Marcotte 2018; Lauzon and Marcotte 2019; Barbosa et al. 2019; Lauzon and Marcotte 2020a; Khambhammettu et al. 2020; Benoit et al. 2020; Lan et al. 2020), to cite a few.

Categorical or multi-facies aquifers are generally constructed using a two-step methodology. First, the hydrofacies are modeled according to available borehole data. Then, the hydrogeological properties of each of the hydrofacies are generated to account for spatial correlations. This raises the issue that the inverse problem matches the state data when the hydrofacies are fixed, which could result in unrealistic parameter values in each of the hydrofacies.

Markov Chain-based methods have been proposed to jointly calibrate hydrofacies and hydraulic conductivity (Alcolea and Renard 2010; Mariethoz et al. 2010a; Hansen et al. 2012). Multi-point models are sampled to maximize the likelihood that the simulated and observed state variables match and corroborate the known facies data. One possibility is the iterative spatial resampling algorithm, in which the transition from one element to the next in the Markov Chain is obtained by transferring the spatial information contained in a random set sampled from the previous simulation and using this set as conditioning data for the next simulation (Mariethoz et al. 2010a). Despite the algorithm's simplicity, it converges too slowly (Khambhammettu et al. 2020) to realistically be used for complex three-dimensional (3D) aquifers.

Recently, authors have proposed using the traveling pilot-point method in conjunction with object-based simulation to parameterize the inverse problem for categorical fields (Khambhammettu et al. 2020). The idea is to adapt the position of pilot points instead of perturbing their values to define the geometries of discrete categories. This has led to two advantages: (i) the categorical problem is restated as a problem with continuous parameters, and (ii) the location of pilot points, and the pilot points help to infer the categories' geometry by object displacement. The traveling pilot point method can be used with pluriGaussian or multi-point simulation. However, developing an appropriate calibration methodology with these two pixel-based algorithms remains a challenge. For example, previously published examples assumes constant hydraulic conductivity within each of the hydrofacies, which is a strong simplification of reality, as a given hydrofacies often has a heterogeneous hydraulic conductivity distribution.

One way to approach the inverse problem for categorical aquifers is to parameterize optimization using only continuous variables modeled by Gaussian or underlying Gaussian random fields. One new variogram-based calibration algorithm, the sequential spectral turning band method (S-STBM), can provide an excellent framework for this purpose. It consists of building an aquifer system from scratch (Lauzon and Marcotte 2020a) and can efficiently handle the categorical inverse problem when combined with pluriGaussian simulation (Lauzon and Marcotte 2022). The method consists of sequentially adjusting each phase of the spectral algorithm to minimize the error between the observed and simulated state data. The S-STBM has been applied in both continuous and discrete domains to inverse problems that calibrate the first arrival travel time between wells and to matching steady-state pressure heads (Lauzon and Marcotte 2020a; Lauzon and Marcotte 2020b; Lauzon and Marcotte 2022). As for categorical problems, a study by Lauzon and Marcotte (2022) showed that the S-STBM is better suited to calibrate state data for categorical problems than the usual calibration methods, such as gradual deformation and iterative spatial resampling. Note that the S-STBM has never been applied to transient head data assimilation.

The proposed methodology uses the S-STBM to jointly calibrate hydrofacies and hydraulic conductivity to state data, in this case, transient pressure head data. To the authors' knowledge, this is the first time that joint calibration is performed to simultaneously determine the uncertainty of hydrofacies and hydraulic conductivity distribution. This paper proposes a method to model and simultaneously calibrate the underlying Gaussian fields of pluriGaussian simulations corresponding to hydrofacies and the Gaussian fields associated with the hydraulic conductivity of each hydrofacies using S-STBM. Parameterization reduces phase vector optimization from multivariate to univariate. The algorithm proposed here is tested on 2D and 3D synthetic aquifers.

The rest of the paper is structured as follows. Section Methodology explains the basis of the methodology. The pluriGaussian simulations and spectral algorithm that are used for conditioning to the borehole data and for the inverse problems are described. A parametrization technique is presented to reduce the multi-dimensional optimization space to a one-dimensional

one. Section Synthetic study presents the flow simulator and the evaluation measures. Section A two-dimensional inversion introduces the 2D synthetic categorical aquifer model and presents the algorithm's technical details. Section Application to a 3D synthetic model illustrates the method's application to a heterogeneous 3D field. The paper ends with a discussion of the main results and the problems encountered.

Methodology

Spectral turning bands method

The spectral turning bands method (STBM) replaces the simulation of a random field in $\mathbb{R}^d$ (in general, $d = 2$ or 3) with a simpler series of simulations in $\mathbb{R}$. Let us consider a d-dimensional stationary continuous covariance $C_d(\mathbf{h})$ whose spectral representation is (Chilès and Delfiner 2012, p. 66):

$$C_d(\mathbf{h}) = \int_{\mathbb{R}^d} e^{i<\mathbf{h},\boldsymbol{\omega}>} d\chi(\boldsymbol{\omega}) = \int_{\mathbb{R}^d} \cos\left(<\mathbf{h},\boldsymbol{\omega}>\right) d\chi(\boldsymbol{\omega}) \tag{1}$$

where $\mathbf{h}$ is a d-dimensional vector specifying a direction, $\boldsymbol{\omega}$ refers to a d-dimensional frequency vector, $<\mathbf{h},\boldsymbol{\omega}>$ is the inner scalar product in $\mathbb{R}^d$ and $d\chi(\boldsymbol{\omega})$ is the spectral measure.

If the covariance matrix, $C_d(\mathbf{h})$, is real and symmetrical around the origin, then so is the spectral measure. Furthermore, if $C_d(\mathbf{h})$ is square integrable, one can express the spectral measure as $d\chi(\boldsymbol{\omega}) = f(\boldsymbol{\omega})d\boldsymbol{\omega}$ where $f(\boldsymbol{\omega})$ is the spectral density (Lantuéjoul 2002). The spectral densities of some common covariance models can be found in Lantuéjoul (2002); Emery and Lantuéjoul (2006); Chilès and Delfiner (2012); Marcotte (2015, 2016); Marcotte and Allard (2017).

Thereafter, let us consider a stationary zero-mean random field $Z(\mathbf{x})$ defined by:

$$Z(\mathbf{x}) = \sqrt{\frac{1}{N}} \sum_{i=1}^{N} \sqrt{2} \cos\left(<\mathbf{V}_i,\mathbf{x}> + 2\pi U_i\right) \tag{2}$$

where $\mathbf{V}$ is a random frequency vector whose distribution is given by the spectral density $f(\boldsymbol{\omega})$ oriented on a unit half d-sphere and $\mathbf{U}$ is a phase vector uniformly distributed on [0, 1]. The random process $Z(\mathbf{x})$ is zero-mean with covariance $C_d(\mathbf{h})$. According to the central limit theorem, $Z(\mathbf{x})$ becomes more ergodic and Gaussian as N increases. The STBM can be implemented sequentially or parallelized. Note that parallelization can be done for each cosine function by computing the coordinate projections on the line with the graphics processing unit (GPU) as suggested by Räss et al. (2019). Also, the STBM: is grid-free, as projection can be performed on any coordinate $\mathbf{x}$; is not limited to small systems, as there is no real memory limitation; and has a complexity of only $O(n)$ where n is the number of simulated points, which makes it tractable for large fields.

Spectral density sampling

The one-dimensional spectral density $f_1(\boldsymbol{\omega})$, with $\boldsymbol{\omega} = \|\boldsymbol{\omega}\|$, defines the distribution of the frequency vector $\mathbf{V}_i$. Matheron (1973) proved that one-to-one mapping between a continuous and isotropic covariance in $\mathbb{R}^d$ and a covariance in $\mathbb{R}$ is possible:

$$C_d(h) = \int_{S^d} C_1(<\mathbf{h},\boldsymbol{\omega}>)\overline{U_d}(d\boldsymbol{\omega}) \tag{3}$$

where $C_d(h)$ is the d-dimensional covariance, $C_1(h)$ is the one-dimensional line covariance associated with $C_d(h)$, with $h = \|\mathbf{h}\|$, S^d is the d-sphere and $\overline{U_d}$ is the uniform distribution over S^d. Note that anisotropic fields can be obtained by dilating, contracting or rotating an isotropic field. This relationship can be used to simulate a Gaussian random field in $\mathbb{R}^d$ through a series of line simulations in $\mathbb{R}$ with covariance $C_1(h)$ or, in this case, a series of spectral bands using the one-dimensional spectral density corresponding to $C_1(h)$.

It is often complicated to relate the covariance function in $\mathbb{R}^d$ to the one in $\mathbb{R}$. However, in d=3, using spherical coordinates makes the relationship simpler. The one-dimensional spectral density $f_1(\boldsymbol{\omega})$ can be easily determined by taking the Fourier transform of the line covariance $C_1(h)$, which is defined as:

$$C_1(h) = \frac{d(hC_3(h))}{dh} \tag{4}$$

$$f_1(\omega) = 2\int_0^{\infty} C_1(h)\cos\left(\boldsymbol{\omega}h\right)dh \tag{5}$$

Another option is to use the Fourier transform of $C_3(h)$ to obtain the spectral density $f_3(\boldsymbol{\omega})$ and then obtain the one-dimensional spectral density $f_1(\boldsymbol{\omega})$ from it:

$$f_3(\omega) = \frac{1}{(2\pi)^3}\int_{\mathbb{R}^3} C_3(h)e^{-i<\mathbf{h},\boldsymbol{\omega}>}dh \tag{6}$$

$$f_1(\boldsymbol{\omega}) = (2\pi\boldsymbol{\omega})^2 f_3(\boldsymbol{\omega}) \tag{7}$$

V can be drawn from a given spectral density by first sampling a random direction v and then uniformly sampling the radial spectral cumulative distribution:

$$F_1(\omega) = \frac{1}{\pi}\int_0^{\omega} f_1(s)ds \tag{8}$$

A uniform 0-1 value b is drawn, and V is obtained with $V = \mathbf{v}F_1^{-1}(b)$ where $\mathbf{v}$ is an oriented unit vector in the d-sphere. Low-discrepancy sequences like the van der Corput sequence (van der Corput 1935) or the Halton sequence

(Halton 1964) can be used to populate the d-sphere more evenly than is possible with purely random drawing (Freulon and de Fouquet 1991; Lauzon and Marcotte 2020a). The van der Corput sequence is used in the algorithm described here.

Number of cosine functions used

In the STBM, it is suggested to generate hundreds of randomly oriented bands (Tompson et al. 1989; Freulon and de Fouquet 1991) to reproduce covariance models with linear behavior at the origin. However, it is more complicated to adequately represent the covariance function in the spectral counterpart. Some authors (Lantuéjoul 2002; Emery and Lantuéjoul 2006; Chilès and Delfiner 2012; Marcotte 2016) suggest using several hundred to several thousand cosine functions to help sample the high frequencies for covariance models with linear behavior at the origin. For smooth covariance functions, such as the cubic or Gaussian models, the STBM generally requires hundreds of cosine functions (Lantuéjoul 2002).

The classical S-STBM calibration algorithm

The S-STBM (Lauzon and Marcotte 2020a; Lauzon and Marcotte 2020b) works essentially the same as an STBM except that the phases are chosen sequentially using optimization to assimilate as many state variables as possible. Eq. 2 can be rewritten in a sequential manner as follows:

$$Z_i(\mathbf{x}) = \sqrt{\frac{i-1}{i}} Z_{i-1}(\mathbf{x}) + \sqrt{\frac{1}{i}}\sqrt{2}\cos\left(< \mathbf{V}_i, \mathbf{x} > + 2\pi U_i\right) \tag{9}$$

Then, the classical S-STBM algorithm can be summarized as follows:

1. Pre-processing step
   - Compute the one-dimensional spectral density f_1 associated with the covariance matrix in question (C_d).
   - Generate an exhaustive set of line directions $\{\mathbf{v}\}$ over the unit half d-sphere using a quasi-random sequence and keep the directions in a list.
   - Set i to 0, Z_0 to a null field, and the condition to false.
2. While the condition is false
   - Increase i by one increment.
   - Select the ith element in the line directions list, namely, $\mathbf{v}_i$.
   - Randomly sample frequency $\boldsymbol{\omega}_i$ from the radial spectral density $f_1(\boldsymbol{\omega}_i)$.
   - Compute the frequency vector $\mathbf{V}_i = \boldsymbol{\omega}_i \mathbf{v}_i$.
   - Determine the phase U_i in Eq. 9 that minimizes the objective function using a line search minimizer (e.g., golden-section search).
   - Compute Z_i using Eq. 9.
   - Verify the stopping criteria. If one is satisfied, set the condition to true.
3. Return Z_i, the calibrated field.

Conditioning to hydrogeological properties

The conditioning of stationary Gaussian random fields to a set of hydrogeological parameters is efficiently handled using simple kriging, namely post-conditioning by simple kriging (Journel 1974; Chilès and Delfiner 2012). It is performed before transforming the Gaussian fields to the marginal distribution of data, solving the flow simulator and evaluating the objective function.

Given an unconditional simulation $Z_u(\mathbf{x})$ and a set of observed Gaussian-transformed hydrogeological data $Z(\mathbf{x}_i), \forall i = 1, ..., N$, post-conditioning can be done using the following classical equation:

$$Z_c(\mathbf{x}) = Z_u(\mathbf{x}) + (Z^*(\mathbf{x}) - Z_u^*(\mathbf{x})) \tag{10}$$

where $(Z^*(\mathbf{x}) - Z_u^*(\mathbf{x}))$ is the difference between the kriging prediction using the set of observed data $Z^*(\mathbf{x})$ and the kriging prediction using the set of unconditional data from the observed data location $Z_u^*(\mathbf{x})$.

PluriGaussian simulations

The idea behind pluriGaussian methods is to combine two or more underlying Gaussian random fields (U-GRFs) simulated over the area of interest and assign them categories according to the values simulated at each point (Armstrong et al. 2011). Assignment leads to the categorical field $C(\mathbf{x})$ and is done using a partitioning rule, $P : \mathbb{R}^P \rightarrow \mathbb{N}$, that transforms a vector formed of P underlying fields into a categorical field. The function $\mathcal{P}$ takes a coordinate $\mathbf{x}$, forms a vector with the respective values of the P underlying fields at coordinate $\mathbf{x}$, and returns a categorical variable.

$$P(\mathbf{Z}(\mathbf{x})) : \left(Z_1(\mathbf{x}), Z_2(\mathbf{x}), ..., Z_P(\mathbf{x})\right) \rightarrow C(\mathbf{x}) \tag{11}$$

PluriGaussian simulation is a flexible method that can be used to simulate a wide variety of aquifer architectures. For example, it can accommodate (non-stationary) facies proportions that vary in different directions by spatially adapting the truncation rule (Emery 2007; Armstrong et al. 2011; Doligez et al. 2015). Also, it makes it possible to represent cyclicity in depositional sequences using correlated and shifted GRFs (Armstrong et al. 2011; Le Blévec et al. 2017). In reservoir engineering, it can be used to model (separately) reservoir architecture and diagenesis (Renard et al. 2008).

For simplicity, but without loss of generality, only stationary cases with uncorrelated U-GRFs are considered.

Conditioning to hydrofacies observed in boreholes

Traditionally, U-GRFs are conditioned to observed hydrofacies, $C(\mathbf{x}_a)$ for $a = 1, ..., A$, using the Gibbs sampler. This method is widely known to be slow when an abundance of data is available, i.e., A is greater than, say, 100,000 (Marcotte and Allard 2018).

Lauzon and Marcotte (2020b) have proposed an alternative to quickly constrain U-GRFs to inequality constraints. Instead of imposing random Gaussian values that follow the partitioning rule at coordinates $\mathbf{x}_a$ and gradually introducing the spatial correlation as in the Gibbs sampler, one can resort to calibrating with the S-STBM, which preserves the correlation structure and seeks to gradually impose the inequality constraints. This results in random fields where $P\big(\mathbf{Z}(\mathbf{x}_a)\big) : \big(Z_1(\mathbf{x}_a), Z_2(\mathbf{x}_a), ..., Z_P(\mathbf{x}_a)\big) \rightarrow C(\mathbf{x}_a)$.

The objective function to be minimized is defined as follows: the domain $D(P_j)$ refers to each Gaussian vector $\mathbf{W} \in \mathbb{R}^P$ that gives facies j (Eq. 12) when $P(\mathbf{W})$ is applied. The boundary of the domain $D(P_j)$ is $S_{D(P_j)}$. The distance between a categorical observation $C(\mathbf{x}_a) = j$ and the Gaussian vector $\mathbf{Z}(\mathbf{x}_a)$ is 0 when $P(\mathbf{Z}(\mathbf{x}_a)) = j$; otherwise it is the minimum Euclidean distance to the boundary $S_{D(P_j)}$. The objective function is the average of these shortest distances (see Eq. 13). Fig. 1 shows a partitioning rule made of three facies and an example of the objective function.

$$D(P_j) = \left\{\forall \mathbf{W} \in \mathbb{R}^P \mid P(\mathbf{W}) = j\right\} \tag{12}$$

$$\begin{aligned} &\mathrm{OF}(\mathbf{Z}) = \tfrac{1}{A}\textstyle\sum_{a=1}^{A} d_a\big(\mathbf{Z}(\mathbf{x}_a) \mid C(\mathbf{x}_a) = j\big) \text{where} \\ &d_a\big(\mathbf{Z}(\mathbf{x}_a) \mid C(\mathbf{x}_a) = j\big) = \begin{cases} \min\limits_{\mathbf{z} \in S_{D(P_j)}} \left\{\mathrm{dist}\big(\mathbf{Z}(\mathbf{x}_a), \mathbf{Z}\big)\right\} & \text{if } \mathbf{Z}(\mathbf{x}_a) \notin \mathcal{D}(\mathcal{P}_j) \\ 0 & \text{otherwise} \end{cases} \end{aligned} \tag{13}$$

where A is the number of categorical observations. Only underlying Gaussian values at borehole locations are simulated conditionally to the inequality constraints. Post-conditioning by simple kriging (see Section The classical S-STBM calibration algorithm) is used to condition the U-GRFs to those values. Therefore, the categories observed in boreholes are reproduced exactly in all simulated aquifers.

Joint calibration of hydrofacies and hydraulic conductivity

The methodology consists of modeling the aquifer facies architecture using pluriGaussian simulation. The U-GRFs of the pluriGaussian simulation and the Gaussian fields associated with the hydrogeological properties are then simultaneously calibrated to assimilate state variables. The study is restricted to the joint calibration of hydrofacies and hydraulic conductivity to transient head data. However, the methodology may be applied to any hydrogeological properties needed to model an aquifer or any state variables, such as particle travel time and the concentrations obtained from tracer tests.

Forcing ergodicity and limiting the number of flow simulator calls

Running a flow simulator is computationally time-consuming, especially for 3D problems. The number of calls made to the flow simulator must therefore be kept low to obtain calibrated models in an acceptable time frame (Saetrom and Omre 2013). As hundreds or thousands of phases are required to ensure the ergodicity of the Gaussian fields when using STBM, many calls to the flow simulator are needed just to avoid banding artifacts.

One, therefore, proposes to generate several (here, M) cosine functions at each iteration. This should avoid any risk of banding and ensure good calibration while minimizing the number of calls to the flow simulator that are required. Eq. 9 then becomes:

$$\begin{aligned} Z_i(\mathbf{x}) = &\sqrt{\frac{(i-1)}{i}} Z_{i-1}(\mathbf{x}) \\ &+ \sqrt{\frac{1}{i}}\sqrt{\frac{1}{M}}\sum_{m=1}^{M}\sqrt{2}\cos\left(<\mathbf{V}_{i,m}, \mathbf{x}> + 2\pi U_{i,m}\right) \end{aligned} \tag{14}$$

where $\mathbf{V}_{i,m}$ and $2\pi U_{i,m}$ are the m^{th} (among M) frequency vector and phase at iteration i, respectively.

Vector phase parameterization

As multiple Gaussian random fields are simulated, the same number of phases (M) needs to be optimized for each field at any given iteration. The number of calls made to the flow simulator may be significantly higher in such conditions than in the univariate case. Also, the discrete nature of the geological models prohibits using gradient-based optimization methods (Hu and Le Ravalec 2004).

The idea is to reduce optimization from multivariate to univariate using parameterization on the phase vector by taking advantage of the building nature of the S-STBM. The gradual deformation scheme is used to achieve this. Two Gaussian white noise vectors of length $(P + Q)$ times M, $\mathbf{z}_1$ and $\mathbf{z}_2$, are fused. Note that $(P + Q)$ refers to the number of Gaussian random fields simulated, with P underlying fields to model the categorical field and Q fields to simulate the hydrogeological properties, and M refers to the numbers of cosine functions (and phases) per field simulated at a given iteration. The Gaussian values are transformed to normal cumulative distribution function values ($G(\cdot)$) that give a set of phases to use in Eq. 2:

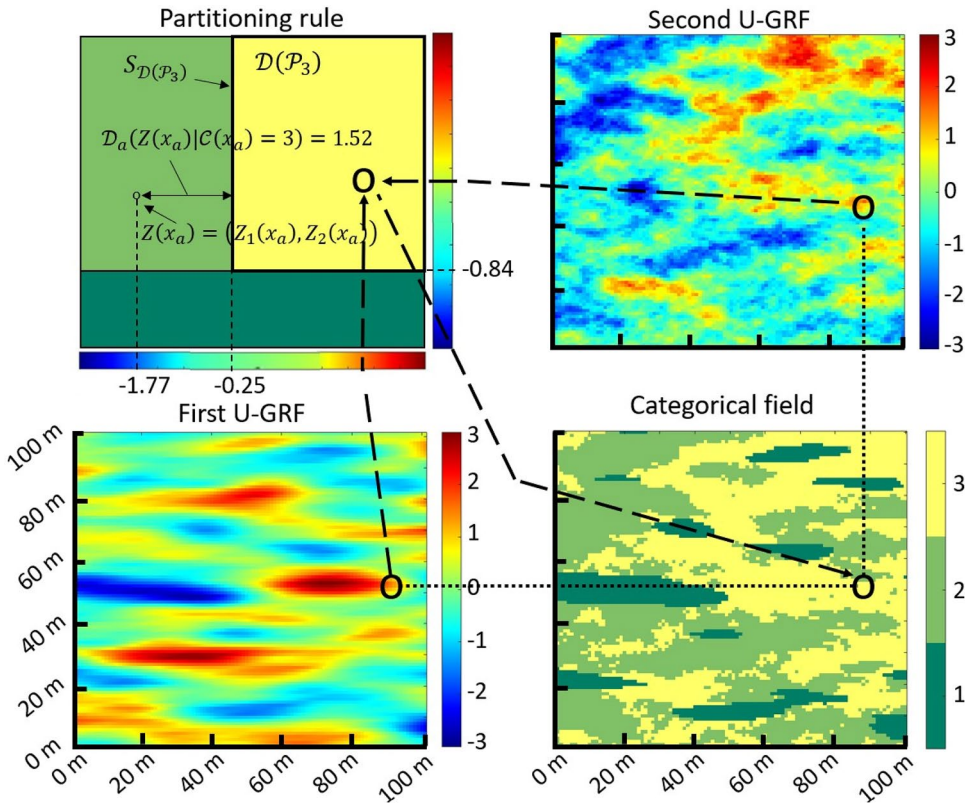

Fig. 1 An example of a pluriGaussian simulation with two uncorrelated U-GRFs. The dashed arrows represent the partitioning produced by Eq. 11. The facies domain ($D(P_3)$), facies boundary ($S_D(P_3)$) and distance ($D_a(\mathbf{Z}(\mathbf{x}_a) \mid \mathrm{C}(\mathbf{x}_a) = 3)$) for the yellow facies numbered 3 are shown in the partitioning rule (see Eq. 12 and Eq. 13)

$$\mathbf{U} = G(\mathbf{z}_1 \cos(t) + \mathbf{z}_2 \sin(t)) \tag{15}$$

As a result, a single continuous variable, t, defined on $[0,2\pi]$ needs to be optimized instead of $P + Q$ times M phases, which significantly reduces the number of calls that need to be made to the flow simulator. Lauzon and Marcotte (2020a) showed that shallow optimization, as is done here with parameterization, at each iteration is a better choice than deep optimization in terms of the objective function (OF) reduction for a fixed number of calls to the direct problem (the flow simulator). t is optimized using a golden-section search with only two iterations ($\beta = 2$), which results in three calls to the flow simulator per iteration with the golden search algorithm. Lauzon and Marcotte (2022) showed that $\beta = 2$ is a better choice than $\beta = \{5, 10, 20\}$ for a fixed number of flow simulator calls in a variety of cases.

Joint calibration algorithm based on S-STBM

If one consider P to denote the number of U-GRFs used in the pluriGaussian simulation scheme, Q to be the number of hydrogeological properties simulated and M to be the number of cosine functions generated, the building sequence of the S-STBM-based algorithm for joint calibration can be summarized as follows:

1. Pre-processing step
   - For i=1, ..., P, generate the underlying Gaussian values for the conditioning of the hydrofacies observed in boreholes (See section PluriGaussian simulations).
   - For i=1, ..., Q, compute the transformation $Y_i = \phi_i(Z_i)$ where Y_i is the hydrogeological property field in original units for property i and Z_i is the Gaussian equivalent for property i. ϕ_i is the transformation associated with property i.
   - For i=1,..., $P + Q$, evaluate the one-dimensional spectral density associated with the prescribed covariance matrix of each underlying field or property field simulated.
   - Generate a list of nIter elements, with nIter being the maximum number of iterations, using a quasi-random sequence. Each element in the list contains $M \times (P + Q)$ line directions, $\{\mathbf{v}\}_{M,P+Q}$, on the unit half d-sphere.
   - Set the P underlying fields and the Q property fields, $Z_{0,i}$ for i=1, ..., $P + Q$, to null fields, and the condition to false.
2. While the condition is false
   - Randomly sample each one-dimensional spectral density M times.
   - Select the i^{th} element of the set $\mathbf{v}_i$ containing $M \times (P + Q)$ line directions.

Table 1 Hydrogeological properties of the three units of the 2D aquifer. ($E[k]$ denotes hydraulic conductivity.)

Facies	Type of soil	$E[k]$ (m/s)	Covariance model	Effective range (m)	Sill
1	Clean sand	1.48E-3	Isotropic exponential	750	0.25
2	Silty sand	2.96E-4	Isotropic exponential	750	0.25
3	Silt	1.97E-6	Isotropic exponential	750	0.25

- Compute the $(P + Q)$ times M frequency vectors.
- Optimize parameter t in Eq. 15 to minimize the mismatch between the observed and simulated state variables.
  - Generate two Gaussian white noise vectors of length $(P + Q)$ times M.
  - Compute the phase vector using Eq. 15.
  - Use the frequencies and phases to compute the P underlying fields and the Q property fields, respectively.
  - If conditioning data are available, perform post-conditioning by kriging (see Sec. The classical S-STBM calibration algorithm and Sec. PluriGaussian simulations).
  - Apply the partitioning rule to the P underlying fields of the pluriGaussian simulation (see Eq. 11) to obtain the hydrofacies.
  - Transform the Q Gaussian fields that correspond to properties using their respective transformation function ϕ_i, and assign the properties to hydrofacies.
  - Run the flow simulator to obtain the simulated state variables.
  - Evaluate the objective function.
- If the objective function is reduced, keep the new fields. Otherwise, keep the fields unchanged.
- Verify the stopping criteria. If one is satisfied, set the condition to true.

3. Return the P underlying fields and the Q property fields associated with the hydrofacies and the simulated properties, respectively.

Synthetic study

The algorithm's performance was tested using a 2D and a 3D synthetic aquifer. The evaluation measures used are the root mean square error of head calibration and the identification of the model parameters, including categorical field and hydraulic conductivity fields reproduction.

Objective function

The objective function measures the root mean square error between the transient heads measured, $h^{\mathrm{m}}_{l,t}$, and those simulated, $h^{\mathrm{s}}_{l,t}$, at each time t for each piezometer l:

$$\mathrm{OF} = \sqrt{\frac{1}{L \times T} \sum_{t=1}^{T} \sum_{l=1}^{L} (h^{\mathrm{m}}_{l,t} - h^{\mathrm{s}}_{l,t})^2} \tag{16}$$

where T is the number of time steps and L the number of piezometers.

Evaluation measures

The percentage of points with coincident simulated and reference hydrofacies, P_{cp}, is used as a performance measure to evaluate the reconstruction of the categorical field and defined as:

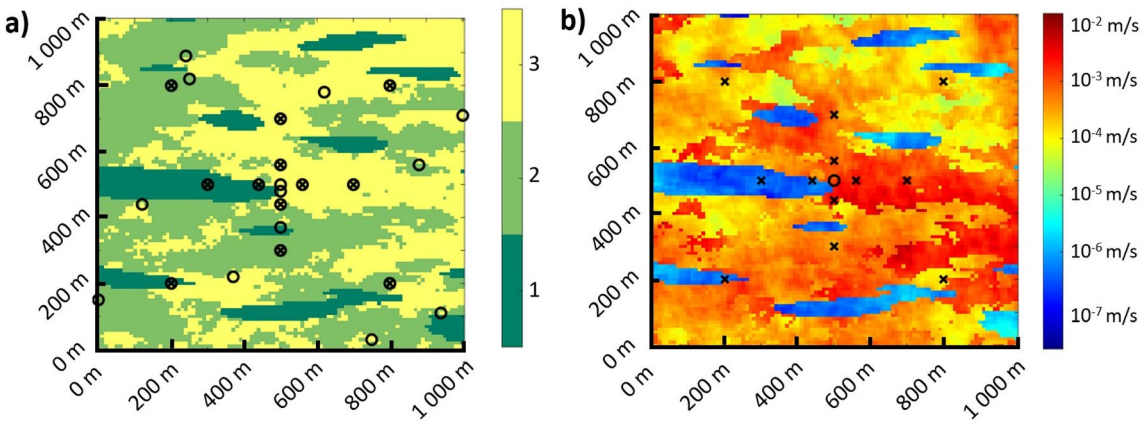

Fig. 2 a) Categorical field and b) $\log_{10}$ hydraulic conductivity field. (Black circles: location of the 24 data collection boreholes—12 at piezometer locations and 12 at randomly sampled locations. Black crosses: location of the 12 piezometers. The pumping well is in the middle of the area.)

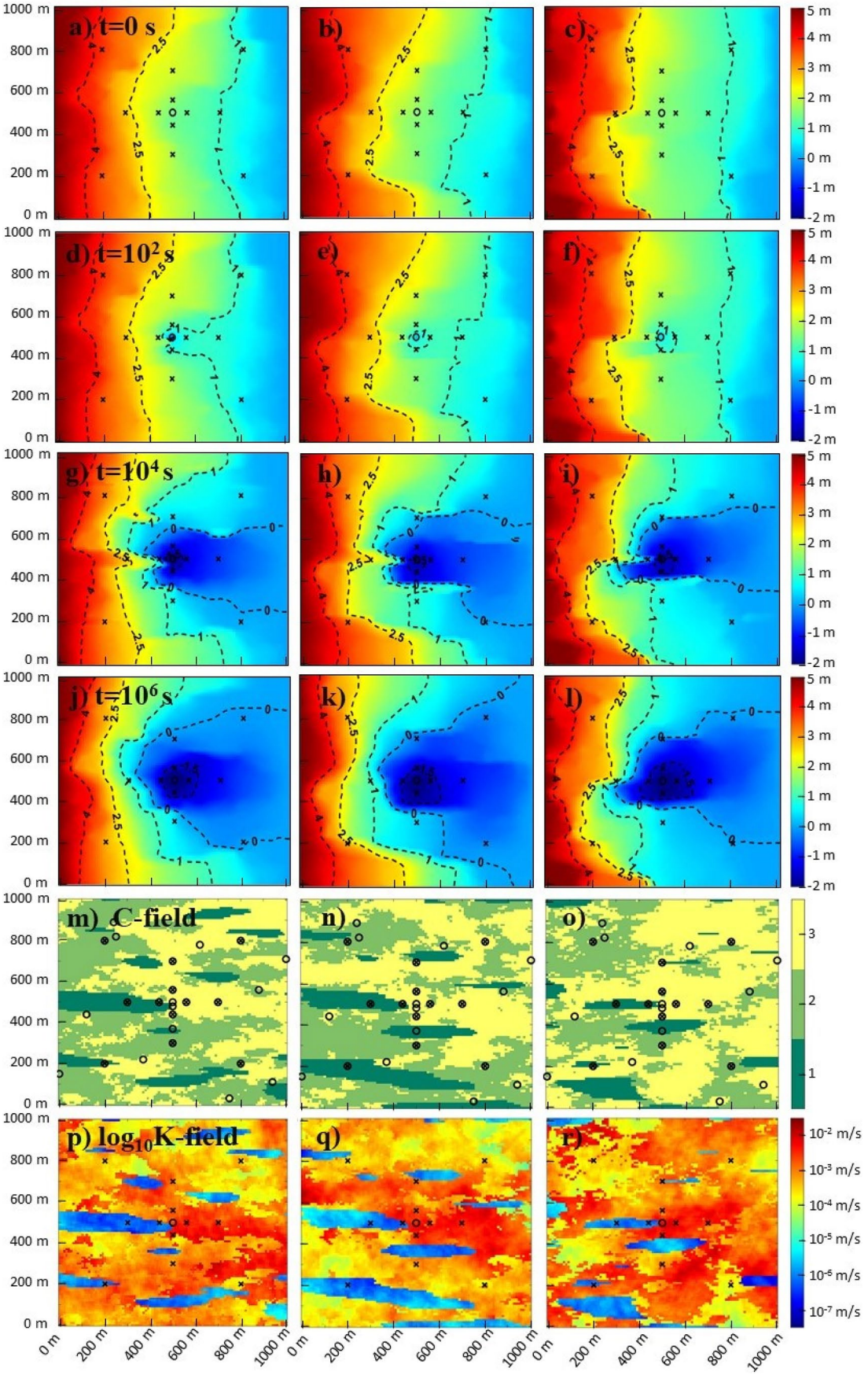
a) t=0 s
b)
c)
d) t=10² s
e)
f)
g) t=10⁴ s
h)
i)
j) t=10⁶ s
k)
l)
m) C-field
n)
o)
p) log10K-field
q)
r)
1000 m
800 m
600 m
400 m
200 m
0 m
5 m
4 m
3 m
2 m
1 m
0 m
-1 m
-2 m
3
2
1
10⁻² m/s
10⁻³ m/s
10⁻⁴ m/s
10⁻⁵ m/s
10⁻⁶ m/s
10⁻⁷ m/s
0 m
200 m
400 m
600 m
800 m
1000 m

◂**Fig. 3** Transient pressure heads at time t =0 s, 10^2 s, 10^4 s, and 10^6 s, categorical field and $\log_{10}$ conductivity field for the reference field (left), Realization 1 (middle), and Realization 2 (right). A total of 24 borehole data points (hydrofacies and hydraulic conductivity) were used for conditioning and 96 transient head data from the 12 piezometers were used for calibration

$$P_{\mathrm{cp}} = \frac{1}{n}\sum_{i=1}^{n} I\left(C^s(\mathbf{x}_i) = C^r(\mathbf{x}_i)\right) \tag{17}$$

where $I(\cdot)$ is the indicator function that has a value of 1 when the condition is verified, C^s is the simulated categorical field, C^r is the reference categorical field, and n is the number of grid points. A higher value indicated a better reconstruction of hydrofacies than a lower value.

Kullback-Leibler divergence, $D_{\mathrm{KL}}(\mathbf{p} \parallel \mathbf{q})$, is used to measure the difference between the probability distribution $\mathbf{p}$ and the reference distribution $\mathbf{q}$. In this case, $\mathbf{q}$ is the vector of hydrofacies proportions in the reference model, while $\mathbf{p}$ as the vector of hydrofacies proportions in the calibrated realizations.

$$D_{\mathrm{KL}}(\mathbf{p} \parallel \mathbf{q}) = \sum_{i=1}^{P} p_i \log\left(\frac{p_i}{q_i}\right) \tag{18}$$

where P is the number of hydrofacies in the pluriGaussian scheme. The closer the value is to zero, the more similar are the proportions of the hydrofacies to the reference.

The correlation between the reference hydraulic conductivity field (K^{r}) and a calibrated hydraulic conductivity field (K^{s}), $\rho(K^{\mathrm{r}}, K^{\mathrm{s}})$, can be used to validate how faithfully hydraulic conductivity was reproduced. Note that correlation is determined using the $\log_{10} K$ fields instead of the original units.

Flow simulator

Hydrogeological inversion was performed using the MATLAB Reservoir Simulation Toolbox (MRST), which is a free open-source software program for modeling hydrogeological systems (Lie 2019). It is worth mentioning that MRST's primary function is not a flow simulator, but rather a research tool for the rapid prototyping of new simulation methods and modeling concepts. It offers a wide variety of easily customizable data structures and pre-programmed methods to model and simulate geological phenomena. In this case, transient head data were obtained by solving a non-linear physical model using automatic differentiation on a regular grid.

Let us consider three-dimensional (or two-dimensional) groundwater flow in a heterogeneous confined aquifer. Under appropriate boundary conditions, the single-phase fluid must satisfy the following continuity equation:

$$\frac{\partial}{\partial t}(\theta\rho_{\mathrm{w}}) + \mathrm{div}\,(\rho_{\mathrm{w}}\mathbf{v}_{\mathrm{D}}) = \rho_{\mathrm{w}}Q_{\mathrm{s}} \tag{19}$$

where θ and ρ_{w} represent the porosity and the density of water, respectively, $\mathbf{v}_{\mathrm{D}}$ is the macroscopic Darcy velocity, and Q_{s} is a source term. That equation represents the conservation of mass. Then, Darcy's law is used to provide the phenomenological relationship between $\mathbf{v}_{\mathrm{D}}$ and fluid pressure p_{f} as follows:

$$\mathbf{v}_{\mathrm{D}} = -\frac{k}{\mu}(\nabla p_{\mathrm{f}} - g\rho_{\mathrm{w}}\nabla z) \tag{20}$$

where k is the permeability, μ is the fluid viscosity, z is the vertical coordinate, and g is the gravitational constant. Note that porosity and fluid density are both functions of fluid pressure (i.e., $\theta(p_{\mathrm{f}})$ and $\rho_w(p_{\mathrm{f}})$). Fluid compressibility (C_{f}), aquifer compressibility (C_{a}), and the storage coefficient (S_{S}) are now introduced to obtain:

$$C_{\mathrm{f}} = \frac{1}{\rho_{\mathrm{w}}}\frac{d\rho_{\mathrm{w}}}{dp_{\mathrm{f}}}; C_{\mathrm{a}} = \frac{d\theta}{dp_{\mathrm{f}}}; S_{\mathrm{S}} = \rho_{\mathrm{w}}g(C_{\mathrm{a}} + C_{\mathrm{f}}\theta) \tag{21}$$

Eq. 20 and Eq. 21 can be used to transform Eq. 19 in terms of hydraulic conductivity (K) and pressure head (h) and obtain:

$$\mathrm{div}\,(-K\nabla h) + Q = S_{\mathrm{S}}\frac{\partial h}{\partial t} \tag{22}$$

Note that $\nabla h = \frac{\nabla p_{\mathrm{f}}}{\rho_{\mathrm{w}}g} - \nabla z$ and $K = \frac{k\rho_{\mathrm{w}}g}{\mu}$. Eq. 22 acts as the governing flow equation in the system.

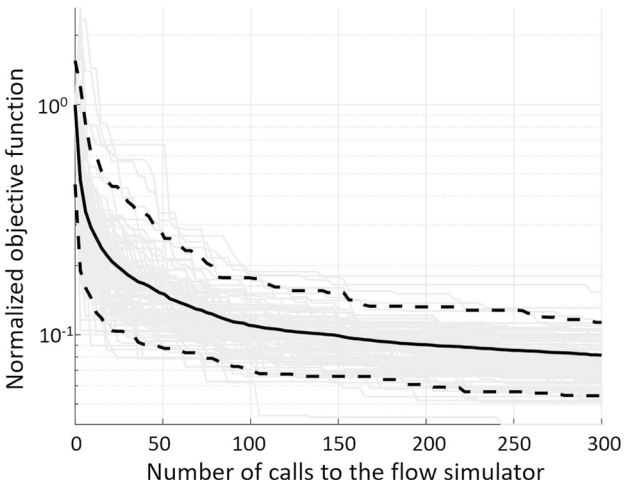

Fig. 4 Normalized objective function. (Solid black line: mean objective function. Gray lines: objective function of 100 realizations. Dashed black lines: 90% confidence interval.)

Table 2 Influence of spatial discretization and the number of nodes on calibration results

Number of nodes (n)	Time to calibrate one realization (min)	Mean (OF_I) without HD (m)	Mean(OF_I) with HD (m)	Mean (OF_F) (m)	Std(OF_F) (m)
2 601	0.21	6.97	3.12	0.25	0.08
10 201	0.55	7.52	2.69	0.22	0.09
22 801	1.21	7.66	2.22	0.22	0.04
40 401	2.40	7.92	2.34	0.24	0.05
90 601	5.67	7.79	2.62	0.25	0.05
160 801	12.05	7.61	2.67	0.27	0.05

(HD: refers to the hydrofacies and hydraulic conductivity data observed in the 24 boreholes. $M = 250$. Realizations: 100. The initial fields were obtained by conditional simulation to HD without transient head calibration.)

A two-dimensional inversion

The synthetic aquifer represents a confined aquifer made of three geological units. The model was obtained by using pluriGaussian simulation with two uncorrelated U-GRFs and applying the partitioning rule illustrated in Fig. 1. The log-conductivity field is shown in Fig. 4b. It measures 1 km × 1 km and is discretized on a 101 × 101 grid. The depth of the aquifer is assumed to be constant throughout the area and set at 1 m. The upper and lower sides are set as no-flow boundaries, and the fixed head boundary conditions are set to 5 m and 0 m on the left and right sides, respectively.

A pumping well with a constant pumping rate of 25 m^3/h is located at the center of the area. The heads obtained at 0 s (initial state), 10^2 s, 10^3 s, 10^4 s, 10^5 s, 10^6 s, 10^7 s and 10^9 s (steady state) over 12 piezometers constitute the conditioning data (96 head data points). The locations of the 12 piezometers (black crosses) and the 24 conditioning data collection boreholes (black circles) are illustrated in Fig. 4a. The conditioning data was collected from 24 boreholes, of which 12 were from piezometer locations and 12 were from randomly sampled locations. The first U-GRF is modeled using anisotropic cubic covariance with a range of a_x=600 m and a_y=100 m. The second U-GRF is modeled using exponential covariance with an effective anisotropic range of a_x =600 m and a_y=300 m. Hydraulic conductivity follows a base-10 log-normal distribution whose parameters are given in Table 1. The conductivity fields are simulated separately (i.e., $Q = 3$) for the different facies. The specific storage, S_S, is set to 1E-4 m^{-1}, and the porosity is set to 0.3 for the three types of hydrofacies.

The reference fields (the two underlying Gaussian fields for the pluriGaussian simulation and the three Gaussian fields for hydraulic conductivity) are sampled from unconditional simulations and have statistics that deviate from the parameters. For example, on average, the partitioning rule induces proportions of 20%, 32% and 48% for hydrofacies number 1, 2 and 3, respectively, whereas the reference proportions are 12.1%, 45.5% and 42.4%, respectively, which represents a deviation of about 6% to 14%. Such large fluctuations are to be expected considering the large correlation range (600 m along the x-direction) of the underlying Gaussian fields compared to the 1000 m extent of the field.

Table 3 Influence of borehole data on calibration results

Case	Number of HD (-)	Mean (OF_I) with HD (m)	Mean (OF_I) (m)	Std (OF_F) (m)	P^I_{cp} (%)	P^F_{cp} (%)	$\overline{\rho(K^r, K^s)_I}$ (-)	$\overline{\rho(K^r, K^s)_F}$ (-)
1	12 (0.12%)	3.80	0.24	0.07	42.9	44.2	0.15	0.20
2	24 (0.25%)	2.69	0.22	0.09	43.5	45.2	0.15	0.17
3	51 (0.5%)	2.42	0.21	0.05	48.5	50.2	0.27	0.28
4	102 (1%)	2.22	0.18	0.05	56.6	57.1	0.36	0.37
5	204 (2%)	1.94	0.15	0.04	63.9	64.1	0.47	0.49
6	357 (3.5%)	0.76	0.13	0.02	72.2	72.4	0.60	0.63
7	510 (5%)	0.72	0.13	0.02	75.8	76.0	0.69	0.72
8	765 (7.5%)	0.72	0.12	0.02	78.9	79.1	0.72	0.75
9	1020 (10%)	0.73	0.12	0.02	81.2	81.3	0.74	0.75

(HD: refers to the hydrofacies and hydraulic conductivity data observed in the boreholes. The mean initial objective function error without HD is the same for all nine cases—7.52 m. The grid size is 101× 101, for 10,201 points.)

Table 4 Joint calibration results. Comparison between the classical sequential approach and joint calibration

Scenario	Conditioning to borehole data	Conditioning to transient data	Joint calibration	P_{cp} (%)	$\overline{\rho(K^r, K^s)}$	$\overline{P_{F_1}}$ (%)	$\overline{P_{F_2}}$ (%)	$\overline{P_{F_3}}$ (%)	$D_{KL}(\mathbf{p} \parallel \mathbf{q}_{ref})$ (%)	$D_{KL}(\mathbf{p} \parallel \mathbf{q}_{HD})$ (%)	Mean(OF) (m)
1	No	No	-	37.0	0.00	20.2	32	47.8	4.82	0.86	7.52
2	Yes	No	-	43.5	0.12	18.7	30	51.3	5.41	0.2	2.69
3	No	Yes	No	37.5	0.03	20.2	30.7	49.1	5.48	0.62	0.45
4	No	Yes	No	40.5	0.05	16.5	32.5	51	3.6	0.27	0.29
5	Yes	Yes	Yes	43.5	0.14	17.8	30.2	52	5.11	0.09	0.27
6	Yes	Yes	Yes	45.2	0.17	16.1	30.1	53.8	4.97	0.03	0.22
Reference	-	-	-	-	-	12.1	45.5	42.4	-	-	-
Borehole Data	-	-	-	-	-	16.7	29.2	54.1	5.61	-	-

Scenario 1: Unconditioned simulations

Scenario 2: Realizations conditioned solely to the 24 borehole data points

Scenario 3: Calibrated to transient heads using a sequential approach without conditioning to the 24 borehole data points

Scenario 4: Joint calibration without conditioning to the 24 borehole data points

Scenario 5: Calibrated to transient heads using a sequential approach with conditioning to the 24 borehole data points

Scenario 6: Joint calibration with conditioning to the 24 borehole data points

The number of iterations was set to 100, which resulted in 300 flow simulator calls per realization (see Sec Joint calibration of hydrofacies and hydraulic conductivity). Fig. 2 shows the categorical fields and the reference $\log_{10}$ hydraulic conductivity field. One hundred realizations were calibrated per test.

First, the results of the inversion are presented. Then, the added value, with respect to hydrofacies identification over the whole field, of combining the hydraulic head information and the hydrofacies observed in boreholes in the inversion is explored.

Joint inversion of a 2D aquifer

Figure 3 shows the head field at various times and the hydraulic conductivity field for the reference field and two calibrated realizations. The main differences observed in the pressure maps appear around the low-conductivity lenses where the head drops are stronger. Despite the small number (24) of known hydrofacies and hydraulic conductivity data points, the hydrofacies and conductivity fields of the two realizations show good agreement with the reference field. The zone of intermediate conductivity located in the upper left corner is relatively well identified, and the one of higher conductivity around the well is present. The low-conductivity hydrofacies of the realizations show some similarities with the reference field, but also noticeable differences in terms of the location and extent of the lenses. By jointly calibrating to transient head data, the percentage of points with coincident simulated and reference hydrofacies ($\overline{P_{cp}}$) increases about 1.7%, from 43.5% (uncalibrated realizations conditioned to borehole data) to 45.2%, on average. Moreover, the mean correlation of the hydraulic conductivity fields ($\overline{\rho(K^r, K^s)}$) increased slightly, from 0.15 to 0.17. Note that the mean OF error is reduced by a factor of 12.22, from 2.69 m to 0.22 m (see the normalized OF, Fig. 4, where 0.22/2.69=0.081).

Impact of field size on calibration

Some calibration algorithms may become less efficient with larger discretization grids caused by a greater number of hydrogeological parameters and more computationally complex optimization schemes (Khambhammettu et al. 2020; Lauzon and Marcotte 2022).The discretization of the grid has therefore been varied from 2,601 nodes (51

Table 5 Hydrogeological properties of the three units of the 3D aquifer. ($E[k]$ denotes hydraulic conductivity.)

Facies	Type of soil	$E[k]$ (m/s)	Porosity (%)	Covariance model	Horizontal range (m)	Vertical range (m)	Sill (-)
1	Silt	6.91E-7	30	Exponential	500	4	0.3
2	Silty sand	1.48E-5	30	Exponential	500	4	0.3
3	Clean sand	1.97E-4	30	Exponential	500	4	0.3

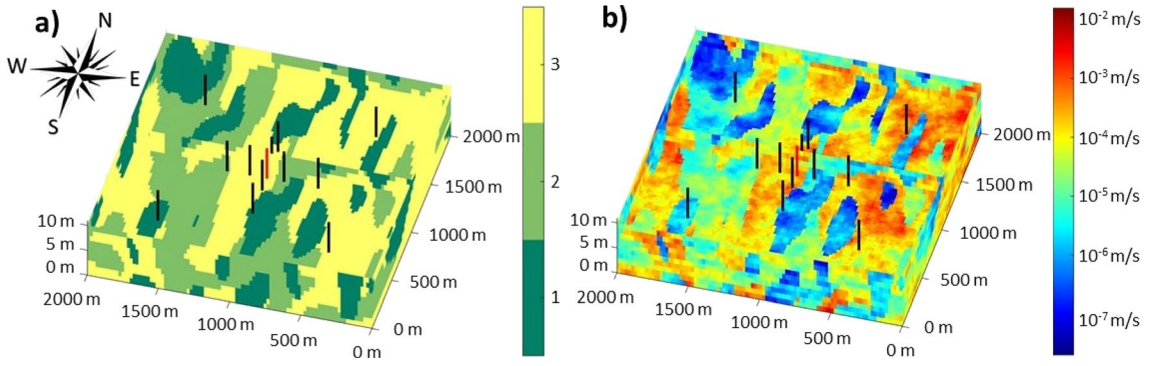

Fig. 5 (a) Categorical field. (b) $\log_{10}$ hydraulic conductivity field. (Black lines: location of the 12 piezometers. Red line: location of the pumping well.)

× 51) to 160,801 nodes (401 × 401). The calibration was performed with the same conditioning data as is used in the previous section. One hundred calibrated realizations were obtained for each grid size.

Table 2 presents the results. The mean initial objective function error (Mean(OF_I)) with and without hard data conditioning, and the mean and standard deviation (Std) final objective function error (Mean(OF_F) and Std(OF_F), respectively) are shown. One note that there is a reduction of one order of magnitude in each case regardless of the discretization size of the field (See Table 2, fifth column). This indicates that the proposed algorithm does not become less efficient when the number of nodes increases, which suggests that it could be applicable to real large-scale three-dimensional studies without loss of efficiency. Note that conditioning to the 24 hard data points alone does not provide acceptable matching between the measured and simulated transient pressure heads.

Influence of borehole data on calibration

This case study seeks to illustrate the influence that hard data—in this case, hydrofacies and hydraulic conductivity observations—have on the calibration of transient pressure head data. Nine scenarios are studied with the following proportions of hard data: 0.12%, 0.25%, 0.5%, 1%, 2%, 3.5%, 5%, 7.5% and 10%. In the 0.12% case, only the data observed at the 12 piezometers were used. The remaining hard data were randomly sampled. The grid size was 101 x 101 for 10,201 points. The results are presented in Table 3. The percentage of points with coincident simulated and reference hydrofacies (P_{cp}) and the $\log_{10}(K)$ mean correlation between the reference field and the one hundred calibrated realizations of the hydraulic conductivity fields ($\rho(K^r, K^s)$) are reported.

When the proportion of hard data used ranges from 0.12% to 2%, a reduction in OF of around one order of magnitude is observed. With more hard data, the initial fields are more constrained by the additional hard data points and the reduction in OF is a bit less. Nevertheless, even with 10% hard data, calibration is able to reduce the OF by a factor six. As expected, the calibrated fields correlate more closely with the reference hydraulic conductivity field, and hydrofacies identification improves as the number of hard data points increases. Note that conditioning to only hard data is not sufficient to reproduce the hydraulic conductivity field at an acceptable level.

Is joint calibration worthwhile?

Six scenarios are studied in order to answer the following two questions: 1) Does jointly calibrating hydrofacies and hydraulic conductivity ensure more accurate identification of the reference model than sequential calibration ? and 2) Do hydraulic head data help improve hydrofacies recognition? The six scenarios are presented in Table 4.

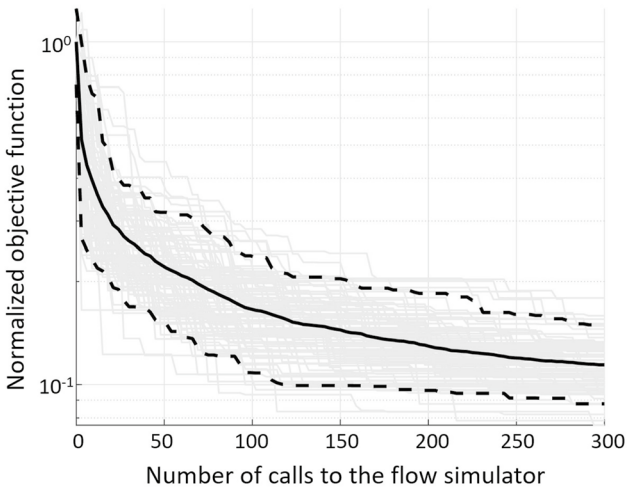

Fig. 6 Normalized objective function. (Solid black line: mean objective function. Gray lines: objective function of 100 realizations. Dashed black lines: 90% confidence interval.)

The first two scenarios are cases without calibration to transient heads. Scenario 1 represents unconditioned simulations, and Scenario 2 depicts realizations conditioned solely to the 24 borehole data points. The third and fourth scenarios are cases in which no borehole data are available. In Scenario 3, the transient heads are calibrated using a sequential approach. First, the hydrofacies are modeled. Then, only hydraulic conductivity is calibrated to match the transient data. In Scenario 4, the proposed joint calibration methodology is used. Scenarios 5 and 6 are identical to Scenarios 3 and 4, respectively, except that they incorporate the 24 borehole data points. Note that one hundred realizations were generated for each scenario. The last two columns of Table 4 present the statistics associated with the reference field and the borehole data. The − symbol indicates that the statistic or result in question could not be computed.

The mean percentage of points with coincident simulated and reference hydrofacies ($\overline{P_{cp}}$), the mean proportions of facies ($\overline{P_{F_1}}$,$\overline{P_{F_2}}$,$\overline{P_{F_3}}$), the mean correlation between the reference field and the hydraulic conductivity fields of the realizations ($\overline{\rho(K^r, K^s)}$), the Kullback-Leibler divergence ($D_{KL}(\mathbf{p} \parallel \mathbf{q})$), and the mean final OF (Mean(OF)) are shown in Table 4.

When Scenarios 3 and 4 and Scenarios 5 and 6 are compared, one can see that joint inversion improves calibration (lower Mean(OF)), hydrofacies identification (higher $\overline{P_{cp}}$), hydraulic conductivity modeling (improved $\overline{\rho(K^r, K^s)}$), and the overall proportion of hydrofacies identified (lower $D_{KL}(\mathbf{p} \parallel \mathbf{q})$).

The Kullback-Leibler divergence (KL) from the reference field ($D_{KL}(\mathbf{p} \parallel \mathbf{q}_{ref})$) is slightly higher for the calibrated Scenarios 3, 5, and 6 than it is for the uncalibrated Scenario 1 but remains less than the KL considering only borehole data vs reference. When KL is computed with the proportions of hydrofacies observed in boreholes ($D_{KL}(\mathbf{p} \parallel \mathbf{q}_{HD})$) and calibration to transient heads is performed, one observe a significant reduction in KL. Therefore, calibrating to transient heads brings the proportion of hydrofacies identified closer to the proportion observed in the borehole data than does Scenario 2, in which no calibration occurs but borehole data are used for conditioning. Moreover, the transient head data were not useful alone in sequential calibration to identify the hydrofacies (37.5% of hydrofacies were correctly identified in Scenario 3 compared to 37% in the unconditioned and uncalibrated realizations of Scenario 1), but it was useful in the joint calibration case (40.5% of hydrofacies were correctly identified in Scenario 4). However, the best results were obtained when combining borehole data and transient head data in the joint calibration approach (Scenario 6), in which case 45.2% of hydrofacies were correctly identified.

Overall, the case study shows that 1) joint calibration provides better results than the classical sequential approach and 2) transient head data is useful to improve hydrofacies identification when used in the joint calibration approach.

Application to a 3D synthetic model

The synthetic model represents a confined aquifer made of three geological units (see Fig. 5a). The model was obtained by using pluriGaussian simulation with two uncorrelated U-GRFs and applying the same partitioning rule as was used in the 2D case (see Fig. 1, top left image). The field measures 2 km × 2 km x 10 m and is discretized on a 101 × 101 x 11 grid (for 112,211 grid nodes). The aquifer's floor, roof, south, and north sides are set as no-flow boundaries, and the fixed head boundary conditions are set to 10 m and 0 m on the east and west sides, respectively.

A pumping well is located at the center of the area and has a constant pumping rate of 25 m^3/h screened from the aquifer floor to its roof. The heads obtained at 0 s (initial state), 10^3 s, 10^4 s, 10^5 s, 10^6 s, 10^7 s, and 10^9 s (steady state) over 12 piezometers constitute the conditioning data (84 head data points). The location of the 12 piezometers (black lines) are illustrated in Fig. 5. Only borehole data are considered in the conditioning data set for hydrofacies recognition and hydraulic conductivity assessment. The boreholes were drilled from the roof to the floor of the aquifer and represent 132 (12 x 11) hydrofacies data points. Hydraulic conductivity data were not used for direct conditioning as, in a real 3D case study, precisely evaluating hydraulic conductivity at a point in a borehole is a complex problem in itself. This additional complexity has been avoided.

The first U-GRF is modeled using anisotropic Gaussian covariance with a range of $a_E = 200$ m, $a_N = 600$ m and $a_v = 8$ m (E: east direction; N: north direction, v: vertical direction). The second U-GRF is modeled using cubic covariance with an effective anisotropic range of $a_E = 400$ m, $a_N = 1600$ m and $a_v = 8$ m. Hydraulic conductivity follows a base-10 log-normal distribution whose parameters are given in Table 5. The number of iterations was set to 100, which resulted in 300 flow simulator calls per realization. Figure 5 shows the categorical fields and the reference $\log_{10}$ hydraulic conductivity field. The conductivity fields are simulated separately (i.e. $Q = 3$) for the different facies.

Joint inversion of a 3D aquifer

One hundred realizations were calibrated using $M = 250$. Figure 6 shows the evolution of the normalized objective function. Normalization is done using the model's mean initial error before calibration and computed on unconditioned realizations. The gray lines represent the 100 realizations; the solid black line is the mean; and the dashed

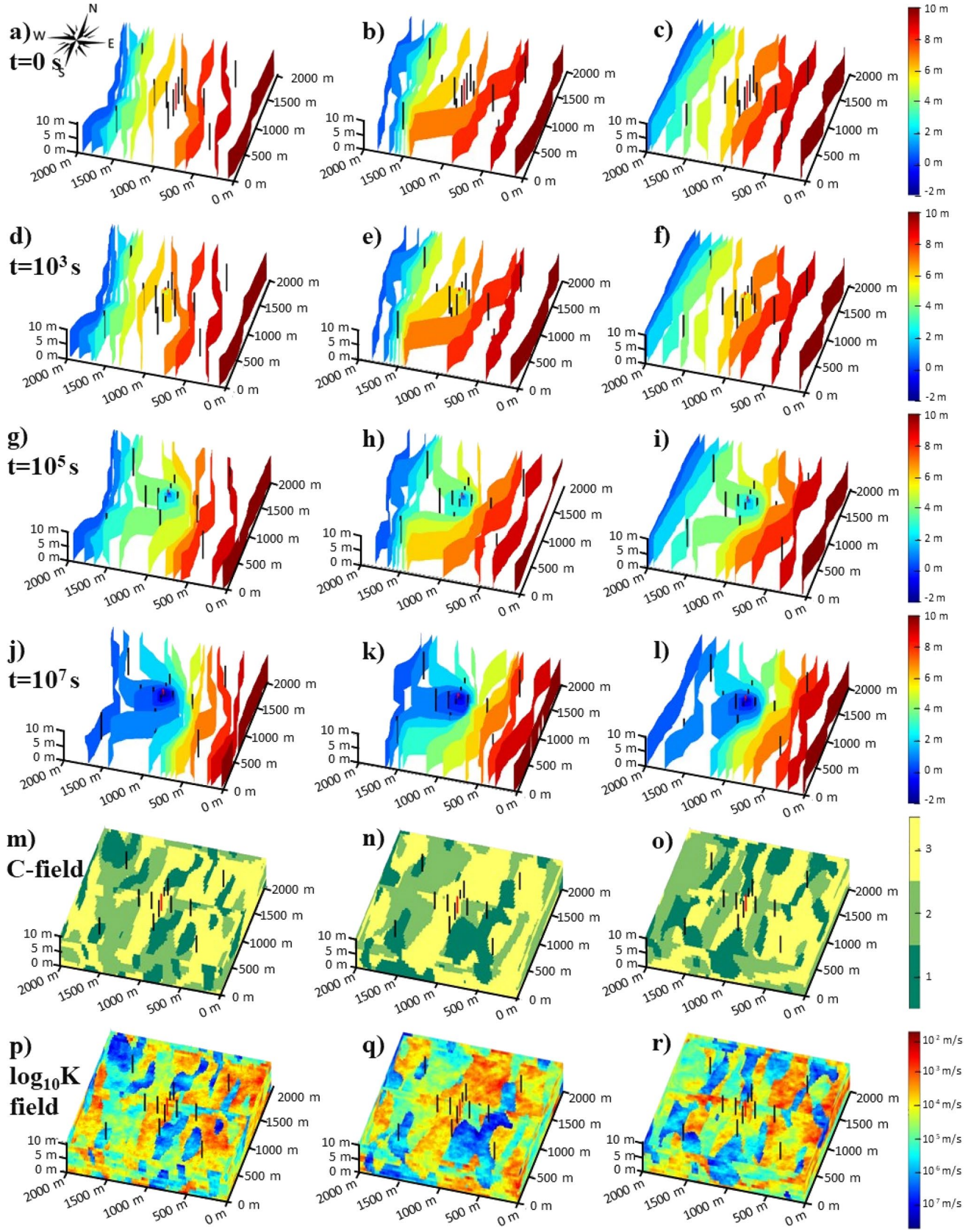
a)
t=0 s
b)
c)
d)
t=10³ s
e)
f)
g)
t=10⁵ s
h)
i)
j)
t=10⁷ s
k)
l)
m)
C-field
n)
o)
p)
log₁₀K
field
q)
r)
N
W
E
S
10 m
5 m
0 m
2000 m
1500 m
1000 m
500 m
0 m
-2 m
3
2
1
10⁻² m/s
10⁻³ m/s
10⁻⁴ m/s
10⁻⁵ m/s
10⁻⁶ m/s
10⁻⁷ m/s

◂**Fig. 7** Transient pressure heads at time $t = 0$ s, 10^3 s, 10^5 s, and 10^7 s, categorical field and log10 conductivity field for the reference field (left), Realization 1 (middle), and Realization 2 (right). A total of 12 borehole data points (or 132 hydrofacies data along the vertical) were used for conditioning and 84 transient head data were used for calibration (12 boreholes x 7 observation times)

black lines are the 90% confidence interval. Despite the complex nature of the aquifer system, calibration achieves a reduction factor of 9, on average, in less than 100 iterations. Note that no realization seems trapped in a local minimum, and the reduction in OF is fast for the initial iterations.

Figure 7 illustrates the head field at various times, the categorical field, and the hydraulic conductivity field for the reference field and two calibrated realizations. The transient hydraulic head fit is good overall. The main differences in the head maps are located close to the boundaries where no data are available to characterize the flow. If one compares subfigures (a), (d), (g), and (j) in Fig. 7 to subfigures (b), (e), (h), and (k), respectively, one can see that drawdowns along the impervious southern boundary occur closer to the western boundary in Realization 1, whereas they are more evenly distributed in the reference field.

The percentage of points with coincident simulated and reference hydrofacies is 46% in the uncalibrated realization and becomes 47% after calibration to the pressure heads. The variation is slight, which indicates that the pressure heads did not help with hydrofacies recognition.

After calibration, Realization 2 ended up with hydraulic conductivity values that were closer to those in the reference field than did Realization 1. In Realization 2 and the reference field, the hydraulic conductivity values are high in the eastern zone and lower in the western zone. However, both Realizations 1 and 2 show similar behavior around the well, with a mix of low conductivity values (Hydrofacies 1) and high conductivity values (Hydrofacies 3). The mean correlation of the calibrated hydraulic conductivity fields and the reference field is slightly higher after calibration (0.08) than before (0.06).

In this scenario, calibration to transient pressure heads was of little help for hydrofacies modeling and hydraulic conductivity identification despite a decrease of close to one order of magnitude in the objective function measuring the match to the transient heads. This result contrasts with the corresponding result in the 2D case, where calibration had a non-negligible impact on the identification of the aquifer's main characteristics. The differences between the 2D case and 3D case may be explained by the much larger number of degrees of freedom for flow in 3D. The transient head data observed at a few wells do not provide as much information as is desired about the aquifer's architecture and the spatial distribution of hydraulic conductivity. Significantly increasing the number of borehole data points or adding auxiliary geophysical data would probably help to improve hydrofacies recognition and hydraulic conductivity assessment, but this may prove to be too costly for the application in question. Nevertheless, the calibrated fields have the obvious advantage of being able to better map the hydraulic head in response to the pumping stress applied, which is useful to identify the capture zone of the pumping well and the flow paths in the event of contamination.

Discussion

In this article, a new approach for the joint inverse modeling of categorical and hydraulic conductivity fields and their associated uncertainties has been proposed. Joint calibration is achieved with Gaussian fields simulated using the spectral method. Calibration to the state variable, transient pressure heads, is done sequentially by adding sets of cosine functions that are shallowly optimized on their phase vectors. In line with the gradual deformation method, the phase vectors are parametrized so as to follow a circular path in $\mathbb{R}^{M(P+Q)}$, which reduces optimization to a one-dimensional process (the position on the circle) and makes it possible to achieve a one-order-of-magnitude reduction in the objective function with a reasonable fixed number of calls to the flow simulator (300 calls per realization). This is an interesting result considering how many parameters need to be calibrated.

Although the number of cosine functions at each iteration was set to $M = 250$, the tests indicate that the results obtained are robust to the value of this parameter, as values of M between 100 and 400 provided similar results. A higher value could potentially generate some realizations that are trapped in a local minimum, and a lower one may not use enough cosine functions to be able to avoid banding artifacts and ensure convergence to a Gaussian distribution.

One way to improve the inversion for the state variable is to use an annealing schedule to reduce the parameter M as the iteration number increases, similarly to the FFTMA-SA method (Lauzon and Marcotte 2019) or the phase annealing algorithm (Yan et al. 2020). However, the use of annealing is nontrivial, and doing so requires several tries to tune its parameters. The experience indicates that an annealing schedule is useful when more than one thousand iterations are carried out. It makes it possible to decrease the intensity of perturbations as calibration progresses (Lauzon and Marcotte 2019; Lauzon and Marcotte 2020b).

The proposed algorithm is an interesting tool for inversion, as it can simultaneously assess the uncertainty of categorical and continuous parameters. The synthetic cases presented involved the inversion of hydrofacies location and

hydraulic conductivity determination. These are probably the parameters that most influence flow, but several other parameters, like porosity and compressibility, may also be uncertain. The approach can easily handle these uncertain parameters by adjusting the number of underlying Gaussian fields to reflect the number of hydrogeological parameters.

The method proposed should also be applicable to the calibration of other state variables, like contaminant concentration, but this remains to be verified. Further research is also needed to include the uncertainty in the hydrogeological model's boundary conditions. Moreover, it is not clear whether increasing the number of hydrogeological parameters (i.e., the number of Gaussian fields) will result in more calls to the flow simulator being needed to obtain a similar level of calibration, i.e., a reduction in the OF of one order of magnitude.

The main drawback of pluriGaussian simulations lies in identifying the variogram models for the underlying Gaussian fields. One can find several sets of parameters that satisfy the field data. Therefore, it may be difficult to justify using a given variogram model. In practice, geoscientists' geological interpretation or conceptual models help guide variogram model selection. For example, cubic or Gaussian variogram models are suitable to represent silty lenses, as in the presented examples. Moreover, the partitioning rule may impact not only hydrofacies transitions, but also higher-order statistics, which can in turn modify hydrofacies connectivity (Beucher and Renard 2016). The same partitioning rule has been applied throughout this paper (Fig. 1), with the lenses defined by the first Gaussian field and the two areas of sand defined by the second one. This has implications for the geometry of hydrofacies bodies and for hydrofacies relationships. It is recommended that hydrogeologists try different partitioning rules and inspect the visual aspect of simulations to ensure they match the conceptual knowledge. Some strategies may require changing the hydrofacies proportion in a certain direction in accordance with borehole observations (D'Or et al. 2017) or adjusting a complex variogram model using correlated underlying functions and shift operators (Le Blévec et al. 2020). These two strategies can easily be incorporated in the algorithm.

In the synthetic case studies considered, the facies architecture was represented by pluriGaussian simulation. Recent developments in pluriGaussian simulation have made it possible to model spatially variable proportions (Mariethoz et al. 2009; Armstrong et al. 2011; Doligez et al. 2015; Madani and Emery 2016), represent discordant or conformable depositional sedimentation processes and diagenesis geometries (Renard et al. 2008), and model cyclic and rhythmic sedimentary deposits (Le Blévec et al. 2018). The proposed calibration algorithm makes these complex models straightforward to use. The same applies for the classical sedimentary model based on the stacked thickness of facies (Allard et al. 2020), as each facies thickness is represented by a distinct Gaussian field. Hence, the calibration algorithm is versatile.

Conclusion

In this paper, a simple and computationally efficient algorithm was tested to solve transient inverse problems for groundwater modeling. The algorithm relies mostly on the spectral simulation method and calibrates as the fields are constructed. The methodology can jointly invert a series of Gaussian fields associated with the hydrofacies, which are modeled using pluriGaussian simulation, and hydraulic conductivity through a one-dimensional optimization scheme. A one-order-of-magnitude reduction in the OF was achieved with 300 calls to the flow simulator, and synthetic cases showed that the methodology is robust to the discretization adopted and does not get easily trapped in local optima. The fast calibration achieved with the proposed approach makes it possible to quantify the uncertainty associated with the hydrogeological model and favors geological risk assessment. Future research is needed to simultaneously assess the uncertainty of other hydrogeological parameters such as boundary conditions, porosity, and contaminant concentration.

Acknowledgements The authors thank the Natural Sciences and Engineering Research Council of Canada (NSERC) for funding this research

Funding Information This research was made possible by the Natural Sciences and Engineering Research Council of Canada (NSERC) through an NSERC grant (CGS D) awarded to D. Lauzon and an NSERC grant (RGPIN-2015-06653) awarded to D. Marcotte. The authors declare that they have no conflicts of interest

Code availability The MATLAB Reservoir Simulation Toolbox is available at Lie (2019). The MATLAB computer codes for the joint inversion of hydrofacies-hydraulic conductivity are available at https://github.com/Danlauz/JointInversion

References

Alcolea A, Renard P (2010) Blocking moving window algorithm: Conditioning multiple-point simulations to hydrogeological data. Water Resources Research 46(8)

Allard D, D'Or D, Froidevaux R (2011) An efficient maximum entropy approach for categorical variable prediction. European Journal of Soil Science 62:381–393

Allard D, Fabbri P, Gaetan C (2020) Modeling and simulating depositional sequences using latent Gaussian random fields. Mathematical Geosciences 53(4):469–497

Allard D, Froidevaux R, Biver P (2005) Accounting for non-stationarity and interactions in object simulation for reservoir heterogeneity characterization. Geostatistics Banff 2004, Springer Netherlands, pp 155–164

Armstrong M, Galli A, Beucher H, Loc'h G, Renard D, Doligez B, Eschard R, Geffroy F (2011) PluriGaussian simulations in geosciences. Springer, Berlin Heidelberg

Barbosa S, Almeida J, Chambel A (2019) A geostatistical methodology to simulate the transmissivity in a highly heterogeneous rock body based on borehole data and pumping tests. Hydrogeology Journal 27(6):1969–998

Bárdossy A, Hörning S (2015) Random mixing: An approach to inverse modeling for roundwater flow and transport problems. Transport in Porous Media 114(2):241–259

Benoit N, Marcotte D, Boucher A, D'Or D, Bajc A, Rezaee H (2017) Directional hydrostratigraphic units simulation using MCP algorithm. Stochastic Environmental Research and Risk Assessment 32(5):1435–1455

Benoit N, Marcotte D, Molson J (2020) Stochastic correlated hydraulic conductivity tensor calibration using gradual deformation. Journal of Hydrology 594:125880

Beucher H, Renard D (2016) Truncated Gaussian and derived methods. Comptes Rendus Geoscience 348(7):510–519

Carrera J, Alcolea A, Medina A, Hidalgo J, Slooten LJ (2005) Inverse problem in hydrogeology. Hydrogeology Journal 13(1):206–222

Chilés J, Delfiner P (2012) Geostatistics: Modeling spatial uncertainty, 2nd edn. John Wiley & Sons

Chilès JP, Delfiner P (1997) Discrete exact simulation by the Fourier method. In: Baafi EY, Schofield NA (eds) Geostatistics Wollongong '96. Kluwer Academic, Dordrecht, pp 258–269

dell'Arciprete D, Bersezio R, Felletti F, Giudici M, Comunian A, Renard P (2011) Comparison of three eostatistical methods for hydrofacies simulation: A test on alluvial sediments. Hydrogeology Journal 20(2):299–311

Deutsch CV (1992) Annealing techniques applied to reservoir modeling and the integration of geological and engineering (well test) data. PhD thesis, Stanford University

Dietrich CR, Newsam GN (1993) A fast and exact method for multidimensional Gaussian stochastic simulations. Water Resources Research 29(8):2861–2869

Doligez B, Ravalec ML, Bouquet S, Adelinet M, Garner D (2015) A review of three geostatistical techniques for realistic geological reservoir modeling integrating multi-scale data. Bulletin of Canadian Petroleum Geology 63(4):277–286

D'Or D (2003) Spatial prediction of soil properties, the Bayesian Maximum Entropy approach. PhD thesis, Université catholique de Louvain

D'Or D, David E, Walgenwitz A, Pluyaud P, Allard D (2017) Non stationary plurigaussian simulations with auto-adaptative truncation diagrams using the CART algorithm. In 79th EAGE Conference and Exhibition 2017. EAGE Publications BV

Emery X (2007) Simulation of geological domains using the plurigaussian model: New developments and computer programs. Computers and Geosciences 33(9):1189–1201

Emery X, Arroyo D, Porcu E (2016) An improved spectral turning-bands algorithm for simulating stationary vector Gaussian random fields. Stochastic Environmental Research and Risk Assessment 30(7):1863–1873

Emery X, Lantuéjoul C (2006) TBSIM: A computer program for conditional simulation of three-dimensional Gaussian random fields via the turning bands method. Computers & Geosciences 32(10):1615–1628

Freulon X, de Fouquet C (1991) Remarques sur la pratique des bandes tournantes á trois dimensions. Cahiers de géostatistique, Fascicule 1,Centre de Géostatistique, École des Mines de Paris, Fontainebleau, pp 101–117

Gómez-Hernández JJ, Sahuquillo A, Capilla J (1997) Stochastic simulation of transmissivity fields conditional to both transmissivity and piezometric data-I. Theory. Journal of Hydrology 203(1–4):162–174

Halton JH (1964) Algorithm 247: Radical-inverse quasi-random point sequence. Communications of the ACM 7(12):701–702

Hansen TM, Cordua KS, Mosegaard K (2012) Inverse problems with non-trivial priors: efficient solution through sequential Gibbs sampling. Computational Geosciences 16(3):593–611

Hörning S, Bárdossy A (2018) Phase annealing for the conditional simulation of spatial random fields. Computers & Geosciences 112:101–111

Hu, (2000) Gradual deformation and iterative calibration of Gaussian-related stochastic models. Mathematical Geology 32(1):87–108

Hu LY, Le Ravalec M (2004) An improved gradual deformation method for reconciling random and gradient searches in stochastic optimizations. Mathematical Geology 36(6):703–719

Huysmans M, Dassargues A (2009) Application of multiple-point geostatistics on modelling roundwater flow and transport in a cross-bedded aquifer (Belgium). Hydrogeology Journal 17(8):1901–1911

Journel AG (1974) Geostatistics for conditional simulation of ore bodies. Economic Geology 69:673–687

Khambhammettu P, Renard P, Doherty J (2020) The traveling pilot point method. a novel approach to parameterize the inverse problem for categorical fields. Advances in Water Resources 138:103556

Kirkpatrick S, Gelatt CD, Vecchi MP (1983) Optimization by simulated annealing. Science 220(4598):671–680

Lan T, Shi X, Chen Y, Li L, Wu J, Duan L, Liu T (2020) Identification of non-Gaussian parameters in heterogeneous aquifers by a modified probability conditioning method through hydraulic-head assimilation. Hydrogeology Journal 29(2):819–839

Lantuéjoul C (2002) Geostatistical simulation. Springer, Berlin Heidelberg

Lauzon D, Marcotte D (2019) Calibration of random fields by FFTMA-SA. Computers & Geosciences 127:99–110

Lauzon D, Marcotte D (2020) Calibration of random fields by a sequential spectral turning bands method. Computers & Geosciences 135:104390

Lauzon D, Marcotte D (2020) The sequential spectral turning band simulator as an alternative to Gibbs sampler in large truncated- or pluri- Gaussian simulations. Stochastic Environmental Research and Risk Assessment 34(11):1939–1951

Lauzon D, Marcotte D (2022) Statistical comparison of variogram-based inversion methods for conditioning to indirect data. Computers & Geosciences pp 105032

Le Blévec T, Dubrule O, John CM (2016) Hampson GJ (2017) Modelling asymmetrical facies successions using pluri-Gaussian simulations. Geostatistics Valencia 19:59–75

Le Blévec T, Dubrule O, John CM, Hampson GJ (2018) Geostatistical modelling of cyclic and rhythmic facies architectures. Mathematical Geosciences 50(6):609–637

Le Blévec T, Dubrule O, John CM, Hampson GJ (2020) Geostatistical Earth modeling of cyclic depositional facies and diagenesis. AAPG Bulletin 104(3):711–734

Le Ravalec M, Noetinger B, Hu LY (2000) The FFT moving average generator : An efficient numerical method for generating and conditioning Gaussian simulations. Mathematical Geology 32(6):701–722

Lie K-A (2019) An introduction to reservoir simulation using MATLAB/GNU Octave. Cambridge University Press. Title: MRST Transforming research. Accessed date :12, Dec. 2022

Madani N, Emery X (2016) Plurigaussian modeling of geological domains based on the truncation of non-stationary Gaussian random fields. Stochastic Environmental Research and Risk Assessment 31(4):893–913

Marcotte D (2015) TASC 3D : A program to test the admissibility in 3D of non-linear models of coregionalization. Computers & Geosciences 83:168–175

Marcotte D (2016) Spatial turning bands simulation of anisotropic non-linear models of coregionalization with symmetric cross-covariances. Computers & Geosciences 89:232–238

Marcotte D, Allard D (2017) Half-tapering strategy for conditional simulation with large datasets. Stochastic Environmental Research and Risk Assessment 32(1):279–294

Marcotte D, Allard D (2018) Gibbs sampling on large lattice with GMRF. Computers & eosciences 111:190–199

Mariethoz G, Renard P, Caers J (2010a) Bayesian inverse problem and optimization with iterative spatial resampling. Water Resources Research 46(11)

Mariethoz G, Renard P, Cornaton F, Jaquet O (2009) Truncated pluriGaussian simulations to characterize aquifer heterogeneity. Ground Water 47(1):13–24

Mariethoz G, Renard P, Straubhaar J (2010) The Direct Sampling method to perform multiple-point geostatistical simulations. Water Resources Research 46(11):W11536

Marsily G, Lavedan G, Boucher M, Fasanino G (1984) Interpretation of interference tests in a well field using geostatistical techniques to fit the permeability distribution in a reservoir model. Geostatistics for natural Resources Characterization, Part 2:831–849

Matheron G (1973) The intrinsic random functions and their applications. Advances in Applied Probability 5(3):439–468

Pasquier P, Marcotte D (2006) Steady- and transient-state inversion in hydrogeology by successive flux estimation. Advances in Water Resources 29(12):1934–1952

Pyrcz M, Boisvert JB, Deutsch CV (2009) ALLUVSIM: A program for event-based stochastic modeling of fluvial depositional systems. Computers & Geosciences 35(8):1671–1685

Renard D, Beucher H, Doligez B (2008) Heterotopic bi-categorical variables in pluriGaussian truncated simulations. VIII International Geostatistical Congress pages 289–298

Rezaee H, Marcotte D (2018) Calibration of categorical simulations by evolutionary gradual deformation method. Computational Geosciences 22(2):587–605

Räss L, Kolyukhin D, Minakov A (2019) Efficient parallel random field generator for large 3-D geophysical problems. Computers & Geosciences 131:158–169

Saetrom J, Omre H (2013) Uncertainty quantification in the ensemble Kalman filter. Scandinavian Journal of Statistics 40(4):868–885

Shinozuka M (1971) Simulation of multivariate and multidimensional random processes. The Journal of the Acoustical Society of America 49(1B):357–368

Shinozuka M, Deodatis G (1996) Simulation of multi-dimensional Gaussian stochastic fields by spectral representation. Applied Mechanics Reviews 49(1):29–53

Shinozuka M, Jan CM (1972) Digital simulation of random processes and its applications. Journal of Sound and Vibration 25:111–128

Strebelle S (2002) Conditional simulation of complex geological structures using multiple-point statistics. Mathematical Geology 34(1):1–21

Tarantola A (2005) Inverse problem theory and methods for model parameter estimation. Society for Industrial and Applied Mathematics

Tompson AFB, Ababou R, Gelhar LW (1989) Implementation of the three-dimensional turning bands random field generator. Water Resources Research 25(10):2227–2243

van der Corput JG (1935) Verteilungsfunktionen (Distribution functions). Akademie van Wetenschappen 38:813–821

Yan J, Bárdossy A, Hörning S, Tao T (2020) Conditional simulation of surface rainfall fields using modified phase annealing. Hydrology and Earth System Sciences 24(5):2287–2301